Journal of the Mechanics and Physics of Solids 61 (2013) 1305–1318

Contents lists available at SciVerse ScienceDirect

Journal of the Mechanics and Physics of Solids

journal homepage: www.elsevier.com/locate/jmps

A new rate-dependent unidirectional composite model – Application to panels subjected to underwater blast

Xiaoding Wei, Alban de Vaucorbeil, Phuong Tran, Horacio D. Espinosa *

Department of Mechanical Engineering, Northwestern University, 2145 Sheridan Road, Evanston, IL 60208-3111, USA

A R T I C L E I N F O

Article history:
Received 23 August 2012
Received in revised form
18 February 2013
Accepted 22 February 2013
Available online 7 March 2013

Keywords:
Damage mechanics
Finite element analysis
Fluid–structure interaction
Underwater blast
Composite failure
Delamination
Material strain rate effects

A B S T R A C T

In this study, we developed a finite element fluid–structure interaction model to understand the deformation and failure mechanisms of both monolithic and sandwich composite panels. A new failure criterion that includes strain-rate effects was formulated and implemented to simulate different damage modes in unidirectional glass fiber/matrix composites. The laminate model uses Hashin's fiber failure criterion and a modified Tsai–Wu matrix failure criterion. The composite moduli are degraded using five damage variables, which are updated in the post-failure regime by means of a linear softening law governed by an energy release criterion. A key feature in the formulation is the distinction between fiber rupture and pull-out by introducing a modified fracture toughness, which varies from a fiber tensile toughness to a matrix tensile toughness as a function of the ratio of longitudinal normal stress to effective shear stress. The delamination between laminas is modeled by a strain-rate sensitive cohesive law. In the case of sandwich panels, core compaction is modeled by a crushable foam plasticity model with volumetric hardening and strain-rate sensitivity. These constitutive descriptions were used to predict deformation histories, fiber/matrix damage patterns, and inter-lamina delamination, for both monolithic and sandwich composite panels subjected to underwater blast. The numerical predictions were compared with experimental observations. We demonstrate that the new rate dependent composite damage model captures the spatial distribution and magnitude of damage significantly more accurately than previously developed models.

1. Introduction

Benefiting from lower material density and with strength comparable to steel, fiber-reinforced composite materials have been widely used in the design of aircrafts, marine hulls, and automobiles under dynamic loadings (Bakis et al., 2002; Lee et al., 2000; Porfiri and Gupta, 2010; LeBlanc and Shukla, 2011; Arora et al., 2011, 2012; Dear et al., 2005; Dear and Brown, 2003). In our previous work (Wei et al., in press), a three-dimensional finite element model was formulated and implemented in ABAQUS (Abaqus 6.9-ef online documentation, 2009) to simulate the deformation and failure of monolithic and sandwich composite panels subjected to underwater blast eliciting fluid–structure interactions (FSI) (Latourte et al., 2011). In such model, the strain-rate effect was modeled for the inter-lamina interface and the foam core in the sandwich panels using a rate-dependent cohesive law and a crushable foam plasticity model, respectively. The model successfully predicted the deformations of both monolithic and sandwich panels over a wide range of water impulses. Furthermore, the model revealed the importance of the foam core in enhancing the energy absorption for sandwich

* Corresponding Author. Tel.: +1 847 467 5989.
E-mail address: espinosa@northwestern.edu (H.D. Espinosa).

0022-5096/$ - see front matter © 2013 Elsevier Ltd. All rights reserved.
http://dx.doi.org/10.1016/j.jmps.2013.02.006

composite panels. However, because the model did not include strain-rate effects on the composite laminate failure, a discrepancy was found for both monolithic and sandwich composite panels when predicting spatial distribution and magnitude of the fiber and matrix damage compared to experimental measurements. Therefore, in order to improve model predictive capabilities and gain a better understanding of the behavior of composite panels under high strain-rate conditions requires the formulation of a more accurate and easy-to-implement model in which material rate-dependence is taken into account.

In this paper, we briefly review the previous numerical model developed to simulate the FSI experiments for monolithic and sandwich composite panels sustaining under-water blast loadings. We then discuss the newly formulated rate-dependent damage model for unidirectional fiber-reinforced composite laminates, including a new failure criterion for orthotropic composite materials based on a modified fracture toughness function for fiber tensile failure. Next, we apply the new model to simulate scaled FSI lab experiments to predict monolithic and sandwich panel deformation and failure. We also compare the new predictions to those obtained in Wei et al. (in press) using Hashin's rate independent model. We close with a discussion of possible future applications of the newly formulated numerical model.

2. Numerical model

Similar to our previous work, the FSI numerical model was implemented in the finite element code ABAQUS/explicit (Abaqus 6.9-ef online documentation, 2009). An Acoustic–Lagrangian (A–L) formulation was used to simulate the fluid–structure interaction. The fluid body was modeled as an acoustic medium with assumptions of inviscid, linear, and compressible mechanical behavior. The interface and foam constitutive formulations used here were previously reported in Wei et al. (in press). The delamination between laminas was modeled by a strain-rate sensitive cohesive law. In the case of sandwich panels, core compaction (H250 PVC) was modeled by a crushable foam plasticity model with volumetric hardening and strain rate. The FSI configuration, boundary conditions, element type and number, as well as model parameters used for the interface and foam materials are the same as those reported in Wei et al. (in press). For the unidirectional fiber-matrix composite, a new rate dependent model was formulated.

2.1. Rate-dependent unidirectional fiber-matrix composite model

2.1.1. Damaged material response

In continuum damage mechanics, as originally proposed by Kachanov (1986), the effect of damage is modeled as a reduction of the stiffness constants. In damage models developed for unidirectional fiber-reinforced composites, e.g., Matzenmiller et al. (1995), reduction of the material's elastic constants is accomplished by introducing five damage variables. To predict the elastic-brittle behavior of unidirectional fiber-reinforced composite plies, Lapczyk and Hurtado (2007) combined the model suggested by Matzenmiller et al. (1995) with Hashin's failure criteria (Hashin and Rotem, 1973; Hashin, 1980). The model differentiates four failure modes: fiber tension, fiber compression, matrix tension, and matrix compression. In the current study, we used an approach similar to that in Lapczyk and Hurtado (2007). Furthermore, as suggested by Chaboche (1981), the effective stress tensor of a material, $\hat{\boldsymbol{\sigma}}$, is defined as the material's responses as if no damage occurs. That is, for a unidirectional composite ply exhibiting orthotropic linear elasticity, the effective stresses in 2D form is defined as

$$\hat{\boldsymbol{\sigma}} = \mathbf{C}_0\boldsymbol{\varepsilon} \quad \text{i.e.,} \begin{bmatrix} \hat{\sigma}_{11} \\ \hat{\sigma}_{22} \\ \hat{\sigma}_{12} \end{bmatrix} = \frac{1}{1-\nu_{12}\nu_{21}} \begin{bmatrix} E_{11} & \nu_{21}E_{11} & 0 \\ \nu_{12}E_{11} & E_{22} & 0 \\ 0 & 0 & (1-\nu_{12}\nu_{21})G_{12} \end{bmatrix} \begin{bmatrix} \varepsilon_{11} \\ \varepsilon_{22} \\ \varepsilon_{12} \end{bmatrix}, \tag{1}$$

where $\mathbf{C_0}$ is the stiffness matrix of the undamaged material. The notation used in Eq. (1) refers to the coordinate system in which the 1-axis and 2-axis are parallel and transverse to the fiber direction, respectively. After damage initiation, the constants in the stiffness matrix decrease to account for the material's degradation. The nominal stress tensor of the damaged material takes the form

$$\boldsymbol{\sigma} = \mathbf{C}\boldsymbol{\varepsilon}, \tag{2}$$

where $\mathbf{C}$ is the stiffness matrix of the damaged material, which can be expressed as

$$\mathbf{C} = \mathbf{M}\mathbf{C_0}\mathbf{M^T}, \tag{3}$$

where $\mathbf{M}$ is the damage operator. In this study, we postulate that $\mathbf{M}$ takes the form

$$M = \begin{bmatrix} \sqrt{1-d_f} & 0 & 0 \\ 0 & \sqrt{1-d_m} & 0 \\ 0 & 0 & \sqrt{1-d_s} \end{bmatrix} \tag{4}$$

where d_f, d_m, and d_s are damage variables for fiber, matrix, and shear failure modes, respectively. Furthermore, similar to the failure modes proposed by Hashin and Rotem (1973) and Hashin (1980), the fiber and matrix damage variables are defined as

$$d_f = \begin{cases} d_{ft} & \text{for} \quad \hat{\sigma}_{11} \geq 0 \\ d_{fc} & \text{for} \quad \hat{\sigma}_{11} < 0 \end{cases}$$
$$d_m = \begin{cases} d_{mt} & \text{for} \quad \hat{\sigma}_{22} \geq 0 \\ d_{mc} & \text{for} \quad \hat{\sigma}_{22} < 0 \end{cases} \quad (5)$$

in which d_{ft} and d_{fc} are the damage variables for fiber tension and compression modes, respectively, and d_{mf} and d_{mc} are the damage variables for matrix tension and compression modes, respectively. The shear damage variable is not independent and takes the form (Lapczyk and Hurtado, 2007)

$$d_s = 1-(1-d_{ft})(1-d_{fc})(1-d_{mf})(1-d_{mc}) \quad (6)$$

All the damage variables take values from zero (no damage) to one (total damage).

2.1.2. Failure criteria

Degradation of unidirectional fiber-reinforced composite materials involves different failure modes such as matrix cracks, fiber-matrix debonds, fiber rupture, and fiber buckling and kinking. Over the past three decades, numerous failure criteria have been developed with the aim to accurately predict the onset of composite material failure. In summary, there are four forms of failure criteria proposed: limit theories (e.g., maximum stress and maximum strain criteria, Rowlands, 1985); polynomial theories (Tsai–Wu failure criterion, Tsai and Wu, 1971, in which a polynomial of stress terms was used to describe a failure surface); strain energy theories (Tsai–Hill, Azzi and Tsai, 1965) failure criterion which used a nonlinear energy based criterion to define material failure); and direct mode theories (Hashin failure criterion, Hashin and Rotem, 1973; Hashin, 1980) in which separate equations are used to describe the onset of each failure mode). Because such model is able to distinguish damage initiation in various failure modes, Hashin failure criterion has been widely used in commercial codes. The failure surface functions that determine the onset of damage in Hashin failure criterion are given by,

Fiber tension failure ($\hat{\sigma}_{11} \geq 0$)

$$F_{ft} = \left(\frac{\hat{\sigma}_{11}}{X^T}\right)^2 + \alpha\left(\frac{\sigma_{12}}{S^L}\right) = 1$$

Fiber compression failure ($\hat{\sigma}_{11} < 0$)

$$F_{fc} = \left(\frac{\hat{\sigma}_{11}}{X^C}\right)^2 = 1$$

Matrix tension failure ($\hat{\sigma}_{22} \geq 0$)

$$F_{mt} = \left(\frac{\hat{\sigma}_{22}}{Y^T}\right)^2 + \left(\frac{\sigma_{12}}{S^L}\right)^2 = 1$$

Matrix compression failure ($\hat{\sigma}_{22} < 0$)

$$F_{mc} = \left(\frac{\hat{\sigma}_{22}}{2X^T}\right)^2 + \left[\left(\frac{Y^C}{2S^T}\right)^2 - 1\right]\frac{\hat{\sigma}_{22}}{Y^C} + \left(\frac{\hat{\sigma}_{12}}{S^L}\right)^2 = 1 \quad (7)$$

In Eq. (7), $X^T$and X^C are the tension and compression strengths in the fiber direction; $Y^T$and $Y^C$are the tension and compression strengths in the matrix (transverse) direction; and $S^L$and $S^T$are the longitudinal and transverse shear strengths. The coefficient αdenotes the contribution of the shear effect on failure initiation due to fiber rupture. As suggested by Hashin (1980), we set $\alpha = 1$.

In a round-robin study (Davila et al., 2005), prediction of the onset of failure, using Hashin criterion, was found to exhibit some deviations from experimental results, especially in matrix and fiber compression modes (Lapczyk and Hurtado, 2007). To remove this limitation, Daniel et al. (2009a, 2009b) performed multi-axial experiments on unidirectional E-glass/vinylester and carbon/epoxy composite laminates and proposed a new interfiber/interlaminar failure theory (referred to as NU criterion), which showed better agreement with experimental results. In this case, onset of matrix failure is expressed in the form of three subcriteria

Tension dominated matrix failure

$$\left(\frac{\hat{\sigma}_{22}}{Y^T}\right) + \left(\frac{E_{22}}{2G_{12}}\right)^2 \left(\frac{\hat{\sigma}_{12}}{Y^T}\right)^2 = 1$$

Shear dominated matrix failure

$$\left(\frac{\hat{\sigma}_{12}}{S^L}\right)^2 + \frac{2G_{12}}{E_{22}}\frac{\hat{\sigma}_{22}}{S^L} = 1$$

Compression dominated matrix failure

$$\left(\frac{\hat{\sigma}_{22}}{Y^C}\right)+\left(\frac{E_{22}}{G_{12}}\right)^2\left(\frac{\hat{\sigma}_{12}}{Y^C}\right)^2=1 \tag{8}$$

In this model, material properties E_{22} and G_{12} were taken into account for predicting matrix failure. The three functions in Eq. (8) define the failure surface for a matrix in the $\sigma_{22}-\sigma_{12}$ plane. This matrix failure surface acknowledges the increase in shear strength for the matrix under compression. However, continuity at the σ_{12}-axis is not guaranteed since the tension- and shear-dominate failure functions do not necessarily intersect at the same point on the σ_{12}-axis for all matrix materials. This limits the generality of the NU criterion. To overcome this shortcoming, we use the Tsai and Wu (1971) failure criterion. In this model, the failure surface in the matrix plane is expressed in the form

$$F_m=\frac{1}{Y^TY^C}\hat{\sigma}_{22}{}^2+\left(\frac{1}{Y^T}-\frac{1}{Y^C}\right)\hat{\sigma}_{22}+\left(\frac{\hat{\sigma}_{12}}{S^L}\right)^2=1 \tag{9}$$

Because the failure surface function in Eq. (9) contains a linear term of $\hat{\sigma}_{22}$, the contribution from the compression stress in the matrix direction is taken into account. To augment the Tsai–Wu failure criterion to better describe matrix failure when $\hat{\sigma}_{22}$ is compressive, we employ the modification proposed by Sun (2000) consisting of the inclusion of an internal friction coefficient for the matrix materials when failing under compression. Thus, the Tsai–Wu failure criterion in the matrix plane was rewritten into the following two subcriteria

Matrix tension failure ($\hat{\sigma}_{22}\geq 0$)

$$F_{mt}=\frac{1}{Y^TY^C}\hat{\sigma}_{22}{}^2+\left(\frac{1}{Y^T}-\frac{1}{Y^C}\right)\hat{\sigma}_{22}+\left(\frac{\hat{\sigma}_{12}}{S^L}\right)^2=1$$

Matrix compression failure ($\hat{\sigma}_{22}<0$)

$$F_{mc}=\frac{1}{Y^TY^C}\hat{\sigma}_{22}{}^2+\left(\frac{1}{Y^T}-\frac{1}{Y^C}\right)\hat{\sigma}_{22}+\left(\frac{\hat{\sigma}_{12}}{S^L-\eta\hat{\sigma}_{22}}\right)^2=1 \tag{10}$$

The internal friction coefficient η can be identified from off-axis tests. To verify the matrix failure surface predicted by Eq. (10), we employed the experimental results by Daniel et al. (2009b) on unidirectional E-glass/vinylester plies. Fig. 1 compares the resulting failure envelopes for unidirectional E-glass/vinylester plies in the $\sigma_{22}-\sigma_{12}$ plane. Inputting $Y^T=45$ MPa, $Y^C=-100$ MPa, $S^L=45$ MPa, and $\eta=0.1$, the failure surface predicted by Eq. (10) is in excellent agreement with the experimental results. In addition, the two subcriteria in Eq. (10) assure continuity of the failure envelope at $\hat{\sigma}_{22}=0$, in contrast to the NU criterion expressed in Eq. (8).

In summary, prediction of the onset of fiber damage is achieved in this study using Hashin criterion, and the matrix failure envelope is described by a modified Tsai–Wu criterion. The formulas for the failure initiation criterion implemented in ABAQUS/explicit (Abaqus 6.9-ef online documentation, 2009), through a user-defined material subroutine VUMAT, are listed below

Fiber tension failure ($\hat{\sigma}_{11}\geq 0$)

$$F_{ft}=\left(\frac{\hat{\sigma}_{11}}{X^T}\right)^2+\alpha\left(\frac{\sigma_{12}}{S^L}\right)=1$$

Fiber compression failure ($\hat{\sigma}_{11}<0$)

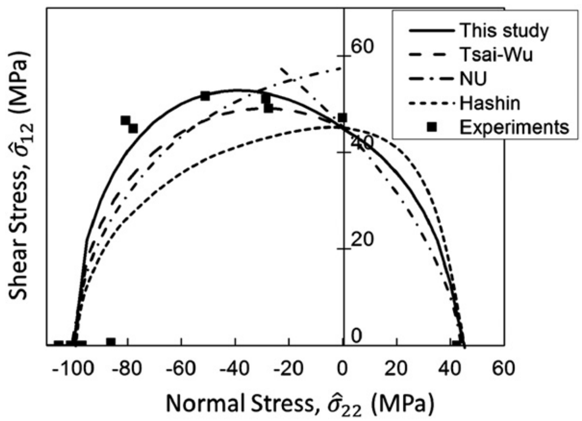

Fig. 1. Comparison of the matrix failure envelopes to the experimental results for E-glass/vinylester composite laminates reported by Daniel et al. (2009b).

$$F_{fc} = \left(\frac{\hat{\sigma}_{11}}{X^C}\right)^2 = 1$$

Matrix tension failure ($\hat{\sigma}_{22} \geq 0$)

$$F_{mt} = \frac{1}{Y^T Y^C}\hat{\sigma}_{22}{}^2 + \left(\frac{1}{Y^T} - \frac{1}{Y^C}\right)\hat{\sigma}_{22} + \left(\frac{\hat{\sigma}_{12}}{S^L}\right)^2 = 1$$

Matrix compression failure ($\hat{\sigma}_{22} < 0$)

$$F_{mc} = \frac{1}{Y^T Y^C}\hat{\sigma}_{22}{}^2 + \left(\frac{1}{Y^T} - \frac{1}{Y^C}\right)\hat{\sigma}_{22} + \left(\frac{\hat{\sigma}_{12}}{S^L - \eta\hat{\sigma}_{22}}\right)^2 = 1 \tag{11}$$

2.1.3. Damage evolution

Complete description of the model requires the definition of damage evolution equations. After the damage initiation criterion is satisfied, further loading will cause degradation of the components in the material stiffness matrix. As shown in Eqs. (3) and (4), reduction of the stiffness constants are realized by increasing the damage variables from zero (no damage) to one (full damage). Camanho and Dávila (2002) proposed that the evolution of the damage variable after the damage initiation should be based on the energy release rate during crack propagation G_C. Linear strain-softening (Lapczyk and Hurtado, 2007; Iannucci and Willows, 2006; Donadon et al., 2008) and exponential strain-softening relationships (Maimí et al., 2006; Tijssens et al., 2000) are the two most common damage evolution laws used to simulate material degradation. In this study and for simplicity, the same linear strain-softening evolution law (Fig. 2) as the one implemented by Lapczyk and Hurtado (2007) is used to model the stress–strain behavior in the post-damage initiation phase.

For a specific damage mode, linear strain-softening yields

$$G_C = \frac{1}{2}\sigma_{eq}^0 \delta_{eq}^f \tag{12}$$

where σ_{eq}^0 is the equivalent strength (i.e., the equivalent stress level at which the failure initiation criterion is satisfied); δ_{eq}^0 denotes the equivalent displacement when the equivalent stress equals σ_{eq}^0; and δ_{eq}^f is the equivalent displacement limit at which the material is fully damaged. The damage variable for each damage mode i is given by

$$d_i = \begin{cases} 0, & \text{for} \quad \delta_{i,eq} < \delta_{i,eq}^0 \\ \frac{\delta_{i,eq}^f(\delta_{i,eq} - \delta_{i,eq}^0)}{\delta_{i,eq}(\delta_{i,eq}^f - \delta_{i,eq}^0)}, & \text{for} \quad \delta_{i,eq}^0 \leq \delta_{i,eq} \leq \delta_{i,eq}^f\,; \\ 1, & \text{for} \quad \delta_{i,eq} > \delta_{i,eq}^f \end{cases}$$
$$\text{where} \quad i \in \{ft, fc, mt, mc\} \tag{13}$$

Similar to the approach in Lapczyk and Hurtado (2007), the mesh dependency problem in the finite element model implementation can be alleviated by setting

$$\delta_{eq}^f = \varepsilon_{eq}^f L_C = \frac{2G_C}{\sigma_{eq}^0} \tag{14}$$

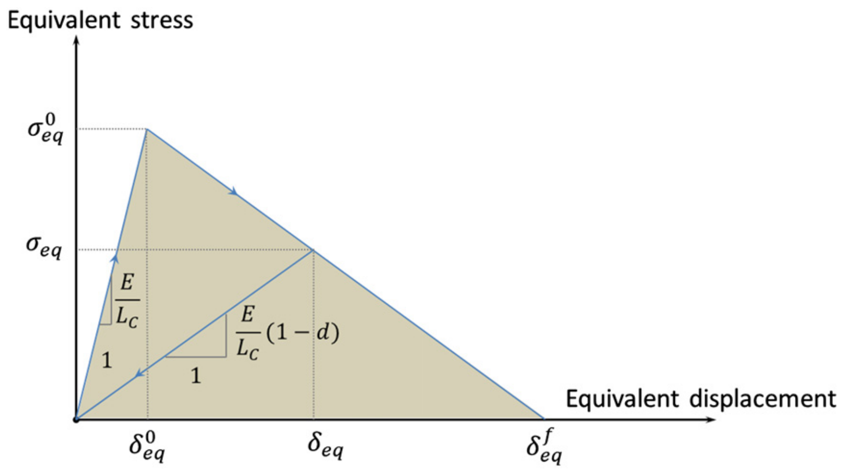

Fig. 2. Damage evolution law for a linearly softening material. The reduced slope in the equivalent plane is given by the reduced modulus divided by the element characteristic length.

Table 1
Equivalent displacements and equivalent stresses, where $\langle\,\rangle$ is the Macauley bracket operator, defined for any $x \in R$ as $\langle x \rangle = \frac{x+|x|}{2}$.

Failure Mode	δ_{eq}	σ_{eq}
Fiber tension ($\hat{\sigma}_{11} \ge 0$)	$L_C\sqrt{\langle \varepsilon_{11}\rangle^2 + \alpha\varepsilon_{12}{}^2}$	$\sqrt{\langle \hat{\sigma}_{11}\rangle^2 + \alpha\hat{\sigma}_{12}{}^2}$
Fiber compression ($\hat{\sigma}_{11} < 0$)	$L_C\langle -\varepsilon_{11}\rangle$	$\langle -\hat{\sigma}_{11}\rangle$
Matrix tension ($\hat{\sigma}_{22} \ge 0$)	$L_C\sqrt{\langle -\varepsilon_{22}\rangle^2 + \varepsilon_{12}{}^2}$	$\sqrt{\langle \hat{\sigma}_{22}\rangle^2 + \hat{\sigma}_{12}{}^2}$
Matrix compression ($\hat{\sigma}_{22} < 0$)	$L_C\sqrt{\langle -\varepsilon_{22}\rangle^2 + \varepsilon_{12}{}^2}$	$\sqrt{\langle -\hat{\sigma}_{22}\rangle^2 + \hat{\sigma}_{12}{}^2}$

Table 2
Scaling functions for the failure initiation criteria.

Failure mode	f
Fiber tension ($\hat{\sigma}_{11} \ge 0$)	$f_{ft} = \frac{1}{\sqrt{F_{ft}}}$
Fiber compression ($\hat{\sigma}_{11} < 0$)	$f_{fc} = \frac{1}{\sqrt{F_{fc}}}$
Matrix tension ($\hat{\sigma}_{22} \ge 0$)	$\dfrac{\hat{\sigma}_{22}\left(\frac{1}{Y^C}-\frac{1}{Y^T}\right)+\sqrt{\hat{\sigma}_{22}{}^2\left(\frac{1}{Y^T}+\frac{1}{Y^C}\right)^2+4\left(\frac{\hat{\sigma}_{12}}{S^L}\right)^2}}{2\left[\frac{\hat{\sigma}_{22}{}^2}{Y^TY^C}+\left(\frac{\hat{\sigma}_{12}}{S^L}\right)^2\right]}$
Matrix compression ($\hat{\sigma}_{22} < 0$)	Solution of $f_{mc}{}^2\frac{\hat{\sigma}_{22}}{Y^TY^C}+f_{mc}\left(\frac{1}{Y^T}-\frac{1}{Y^C}\right)\hat{\sigma}_{22}+f_{mc}{}^2\frac{\hat{\sigma}_{12}{}^2}{(S^L-\eta f_{mc}\hat{\sigma}_{22})^2}=1$

where ε_{eq}^f is the equivalent strain at which the material is fully damaged. L_C is the characteristic length of the element, which is equal to the square root of the area associated with an integration point in ABAQUS/explicit (Abaqus 6.9-ef online documentation, 2009). The equivalent displacements and equivalent stresses for each failure mode are listed in Table 1.

The equivalent displacements and equivalent stresses at the onset of damage initiation are computed by

$$\begin{aligned} \delta_{i,eq}^0 &= \delta_{i,eq} f_i \\ \sigma_{i,eq}^0 &= \sigma_{i,eq} f_i, \end{aligned} \tag{15}$$

where f_i is the scaling function for each damage mode ($i \in \{ft,fc,mt,mc\}$). The scaling functions that correspond to the new failure initiation criteria given by Eq. (11) are listed in Table 2. Note that because the onset of the matrix damage is described by the modified Tsai–Wu criteria, the scaling functions for the matrix tension and compression modes are different than those for the Hashin failure criteria implemented in Lapczyk and Hurtado (2007). Furthermore, because of the internal friction coefficient η in the matrix compression failure criterion, a parabolic equation needs to be solved numerically to obtain the scaling function f_{mc}.

Besides modification of the failure criteria, we also re-examined the damage evolution law for fiber damage under tension. In contrast to fiber damage in compression, which is mainly through fiber kinking and buckling, damage to fibers under tension is dominated by modes that cause fiber rupture or pull-out. The latter is primarily caused by in-plane shear deformation. This shear contribution to failure initiation for a fiber under tension is accounted for in Hashin's failure criteria. However, the shear contribution to damage evolution in fiber tension mode was omitted in the implementation in Lapczyk and Hurtado (2007). The same fracture toughness G_C^{ft} is used no matter if the fiber fails in rupture or pull-out, i.e.,

$$\delta_{ft,eq}^f = \varepsilon_{ft,eq}^f L_C = \frac{G_C^{ft}}{2\sigma_{ft,eq}^0} \tag{16}$$

Here we proposed a modification in the fracture toughness for the fiber tension failure mode to account for the shear contribution. When the fibers rupture due to pure normal tensile stress, the fracture toughness is G_C^{ft}; however, when the fibers fail by pull-out due to debonding at the fiber-matrix interface, the fracture toughness should reduce to G_C^{mt}. Therefore, similar to the relationship proposed by Benzeggagh and Kenane (1996) for mixed mode delamination, the fracture toughness for fiber tension damage mode is defined as a function of the ratio between longitudinal normal stress and effective shear stress

$$\tilde{G}_C^{ft} = (G_C^{ft} - G_C^{mt})\sqrt{\frac{\hat{\sigma}_{11}{}^2}{\hat{\sigma}_{11}{}^2 + \alpha\hat{\sigma}_{12}{}^2}} + G_C^{mt} \tag{17}$$

In this study, the modified fracture toughness $\tilde{G}_C^{ft}$ is used to account for the shear contribution to the damage evolution for the fiber tension damage mode.

2.1.4. Strain-rate dependence of strength and toughness

One important characteristic of the finite element model implemented in this study is that the strain-rate dependence of the strength of the fiber-reinforced composites has been accounted for. Experiments have shown that strain rate affects the modulus, strength, and toughness of glass-fiber reinforced composites (Daniel et al., 2009a, 2009b; Oguni and Ravichandran, 2001; Akil et al., 2003; Shokrieh and Omidi, 2009a, 2009b, 2009c; Naik et al., 2010). To preserve model implementation simplicity, the strain-rate effect on a material's modulus was neglected in this study. The rate dependence of the strength of a unidirectional E-glass fiber/vinylester ply in each damage mode is modeled by

$$\begin{aligned}
X^T &= X_0^T\left[m_f \log\left(\frac{|\dot{\varepsilon}_{11}|}{\dot{\varepsilon}_{0,11}}\right)+1\right]\\
X^C &= X_0^C\left[m_f \log\left(\frac{|\dot{\varepsilon}_{11}|}{\dot{\varepsilon}_{0,11}}\right)+1\right]\\
Y^T &= Y_0^T\left[m_m \log\left(\frac{|\dot{\varepsilon}_{22}|}{\dot{\varepsilon}_{0,22}}\right)+1\right]\\
Y^C &= Y_0^C\left[m_m \log\left(\frac{|\dot{\varepsilon}_{22}|}{\dot{\varepsilon}_{0,22}}\right)+1\right]\\
S^L &= S_0^L\left[m_m \log\left(\frac{|\dot{\varepsilon}_{12}|}{\dot{\varepsilon}_{0,12}}\right)+1\right]
\end{aligned} \tag{18}$$

where X_0^T, X_0^C ,Y_0^T, Y_0^C and S_0^L are the reference strengths of fiber tension, fiber compression, matrix tension, matrix compression and in-plane shear, respectively; $\dot{\varepsilon}_{0,11}$, $\dot{\varepsilon}_{0,22}$ and $\dot{\varepsilon}_{0,12}$ are the longitudinal normal, transverse normal and in-plane shear reference strain rates, respectively; m_f and m_m are the strain rate sensitivities for the fiber and matrix modes, respectively. These values can be determined by performing multi-axial dynamic experiments on the unidirectional plies. For unidirectional E-glass fiber/vinylester composite plies, the rate dependence of the strengths for the fiber failure modes was adapted from the dynamic tests by Oguni and Ravichandran (2001). The rate dependence of the strengths for the matrix failure modes was adapted from the dynamic tests by Daniel et al. (2009b). The reference strengths were adapted from quasi-static results (Daniel et al., 1994). To assure stability of the linearly softening damage evolution model, we assumed that the failure strain of the composite has the same rate dependence as the strength. Therefore the toughness of the composite, under dynamic loading, for each damage mode is expressed as

$$\begin{aligned}
G_C^{ft} &= G_{0,C}^{ft}\left[m_f \log\left(\frac{|\dot{\varepsilon}_{11}|}{\dot{\varepsilon}_{0,11}}\right)+1\right]^2\\
G_C^{fc} &= G_{0,C}^{fc}\left[m_f \log\left(\frac{|\dot{\varepsilon}_{11}|}{\dot{\varepsilon}_{0,11}}\right)+1\right]^2\\
G_C^{mt} &= G_{0,C}^{mt}\left[m_m \log\left(\frac{|\dot{\varepsilon}_{22}|}{\dot{\varepsilon}_{0,22}}\right)+1\right]^2\\
G_C^{mc} &= G_{0,C}^{mc}\left[m_m \log\left(\frac{|\dot{\varepsilon}_{22}|}{\dot{\varepsilon}_{0,22}}\right)+1\right]^2
\end{aligned} \tag{19}$$

The parameters used in modeling the dynamic behavior of the E-glass fiber/vinylester composite panel are listed in Table 3.

The rate-dependent progressive damage model discussed in the previous section was then implemented using VUMAT for unidirectional fiber-reinforced composites. In the implementation, at the beginning of strain step, information such as the previous strain tensor, the strain increment tensor in the current step, the time increment for the current step, etc., are passed into the VUMAT subroutine. The strain rate tensor is calculated and then used to update the strength and toughness of the composite for each damage mode. In the meantime, the effective stress tensor is updated and input, along with the

Table 3
Material properties of dynamic behavior for E-glass/vinylester unidirectional composite.

Material property	Value	Material property	Value
Density, ρ	1850 kg/m^3	X_0^T	1.2 GPa, Daniel et al. (1994)
E_{11}	39 GPa, Daniel et al. (1994)	X_0^C	620 MPa, Daniel et al. (1994)
E_{22}	11.5 GPa, Daniel et al. (1994)	Y_0^T	45 MPa, Daniel et al. (2009b)
G_{12}	3.5 GPa, Daniel et al. (1994)	Y_0^C	100 MPa, Daniel et al. (2009b)
Poisson's ratio, v	0.28, Daniel et al. (1994)	S_0^L	45 MPa, Daniel et al. (2009b)
m_f	0.177, Oguni and Ravichandran (2001)	$G_{0,C}^{ft}=G_{0,C}^{fc}$	35×10^3 N/m, Roy et al. (2001)
m_m	0.2, Daniel et al. (2009b)	$G_{0,C}^{mt}=G_{0,C}^{mc}$	2×10^3 N/m, Compston et al. (1998)
$\dot{\varepsilon}_{0,11}$	1×10^{-3} s^{-1}Oguni and Ravichandran (2001)	$\dot{\varepsilon}_{0,22}$	1×10^{-3} s^{-1}, Daniel et al. (2009b)

dynamic strength, into the failure criteria equations (Eq. (11)) to check whether the element is damaged. If the failure criteria are satisfied, the linearly softening damage evolution law is applied with the updated toughness. The damage variables for all damage modes are updated and saved as state variables. At the end of each step, the nominal stress tensor is updated and passed back into ABAQUS/explicit.

3. Numerical results and discussion

3.1. Monolithic panels

To assess the performance of the new model, we simulated some of the FSI experiments reported in Latourte et al. (2011). In this regard, the monolithic panel impacted by an impulse of 2425 Pa s gave multiple interesting failure mechanisms such as a complicated inter-lamina delamination pattern and matrix damage pattern (Latourte et al., 2011). The numerical model was applied to recapture those features. First, the central deflection history predicted by the numerical model was compared with the experimental measurement (Fig. 3). A maximum deflection of ~19.6 mm and a final deflection of ~7.0 mm are predicted, which agree well with the experimental values of 19.5 and 6.7 mm, respectively. The deflection rate in the ascending segment (from 0 to 250 μs after the pulse impact) compares favorably

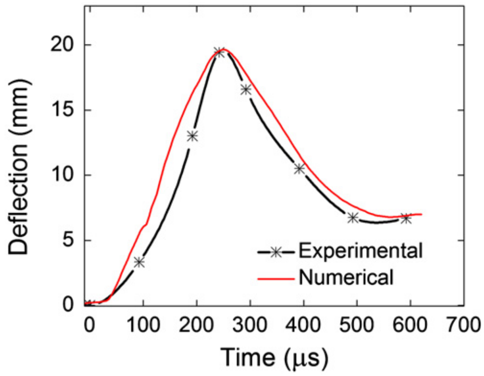

Fig. 3. Experimental central deflection history compared with that predicted by numerical simulations.

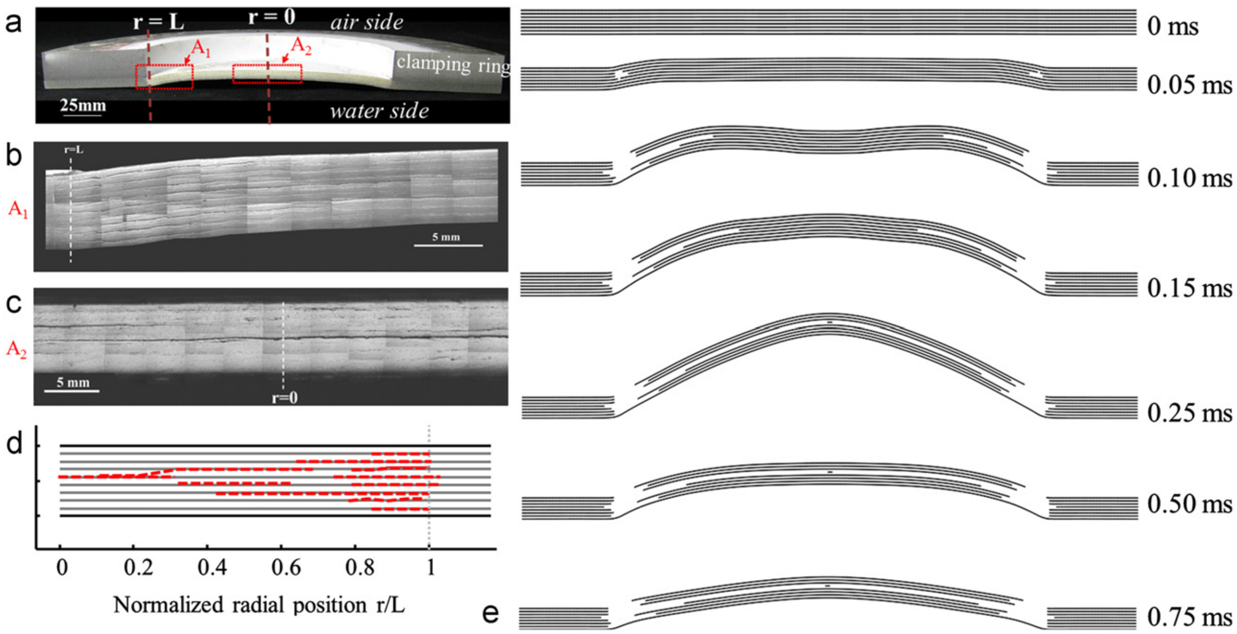

Fig. 4. (a) Cross-sectional view of the monolithic panel #1–3 after the test; (b) and (c) optical micrographs of inter-lamina delamination close to the clamped edge (region A_1 in (a)) and at the center (region A_2 in (a)), respectively; (d) Schematic of the interface delamination pattern along the radial position; and (e) numerically predicted interface delamination history.

with the experimental measurement. In addition, the spring-back of the panel after reaching the maximum deflection is well captured by the simulation.

Moreover, the material failure predicted by the model was compared with the experimental records. The inter-lamina delamination pattern predicted by the numerical model correlates well with the experimental measurement. Micrographs of the cross-section (Fig. 4a–c) reveal characteristic delamination patterns for the monolithic composite panel. At the clamped edge, delamination at all eight interfaces developed due to shearing, with partial propagation to the center of the panel (Fig. 4b). As deformation of the panel increased, a delamination front propagates along the central interface (Fig. 4c and d) depicts the delamination pattern obtained from the specimen after the test. The numerically predicted delamination history is shown in Fig. 4e. Delamination initiates at the clamped boundaries and propagates toward the center. Both the panel deflection and delamination reach their maximum at approximately 0.25 ms. Then a spring back of the panel is observed, and no further delamination is predicted. The final delamination pattern agrees well with the one observed in the experiment (Fig. 4a–d). The predicted delamination pattern in this study is very similar to the one predicted in our previous report (Wei et al., in press) because the same rate-dependent cohesive law was implemented.

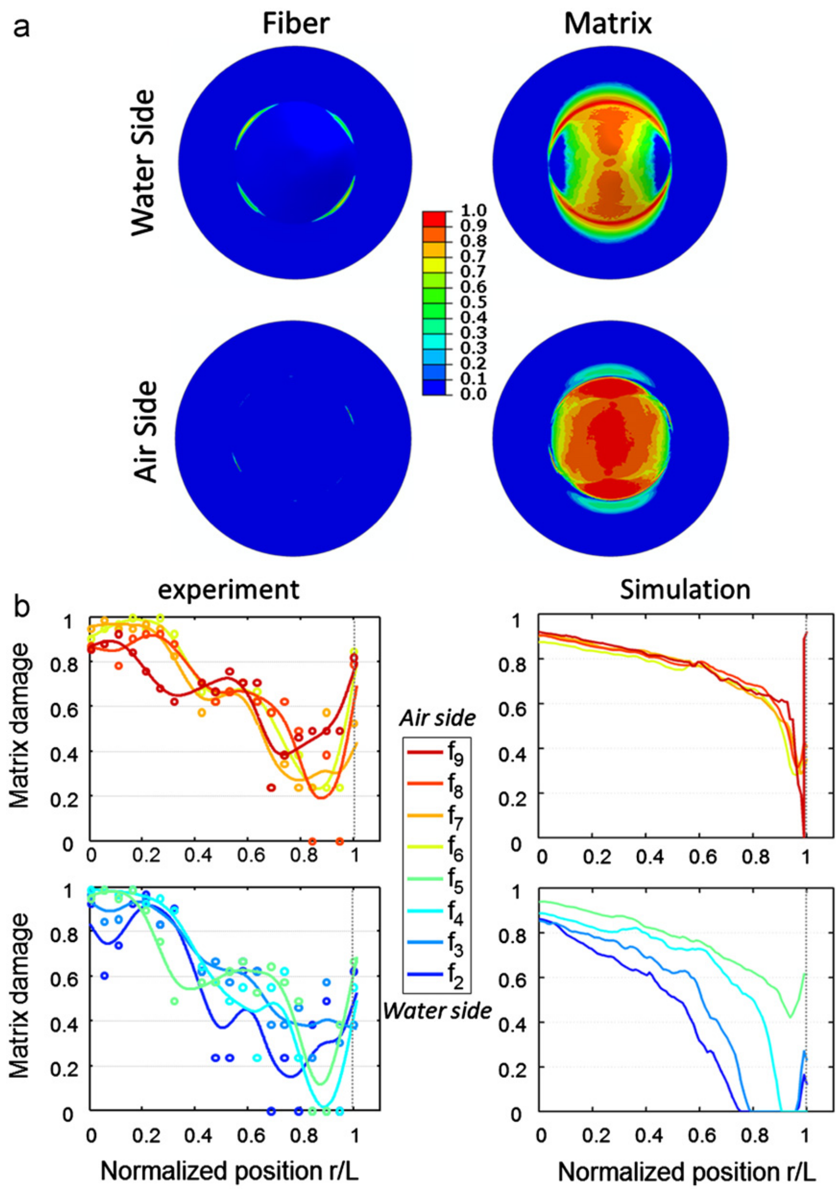

Fig. 5. (a) Fiber and matrix damage patterns in the water-side and air-side laminas for the monolithic composite panel where the damage variable from 0–1 represents the damage level from low to high; (b) comparison of matrix damage variables in individual lamina as a function of panel radial position from experiments and simulations. In this plot, $f_i (i = 1,2,\ldots 9)$ represents the laminas from the water-side to the air-side (the result for f_1 was not given in Latourte et al. (2011) due to extensive noise and uncertainties in the measurements).

Fiber and matrix damage patterns have also been extracted from the simulation results. As shown in Fig. 5a, the fibers on the water-side and air-side laminates begin to show damage, albeit significantly less than the total failure, previously predicted with Hashin's rate independent laminate model (Wei et al., in press), at the clamped edge and outer region, respectively. Thus, the whole panel shows no evidence of fiber catastrophic failure, which agrees well with the experimental observation. Likewise, when comparing simulation results for Hashin's rate independent model and the present model, the matrices in laminates on both sides show similar anisotropic damage patterns but they are much less pronounced in the new model predictions. Moreover, the matrix damage d_m along the radius was extracted from the simulation and compared with the experimental measurements in Latourte et al. (2011) (Fig. 5b). The experiment and simulation follow a similar trend – the matrix damage is maximized at the center due to high bi-axial tension, which becomes more pronounced when the water cavity collapses due to the FSI effect. The matrix damage is reduced toward the clamped edge but is still present due to bending effects. Overall, the matrix damage level predicted by the new rate dependent model agrees much better with that measured experimentally, along the radial distance, than our previous model (Wei et al., in press). This is due to the fact that a more accurate composite failure envelop was used and that rate-dependence for both the composite strength and toughness are taken into account in this study.

3.2. Sandwich panels

The second application of the numerical model we discuss here is the prediction deformation and failure mechanisms for sandwich composite panels in which a soft core is present between the water-side and air-side face sheets. At the same areal weight, the sandwich composite outperforms the monolithic panels by sustaining higher impulses and showing suppressed panel deflections (Latourte et al., 2011). Among the six sandwich composite panels tested in Latourte et al. (2011), the one impacted at an impulse of $I_0=5581$ Pa s is of greatest interest because it exhibited a complex synergy of failure mechanisms, containing foam crushing, initiation of fiber rupture failure, inter-lamina delamination, and signs of

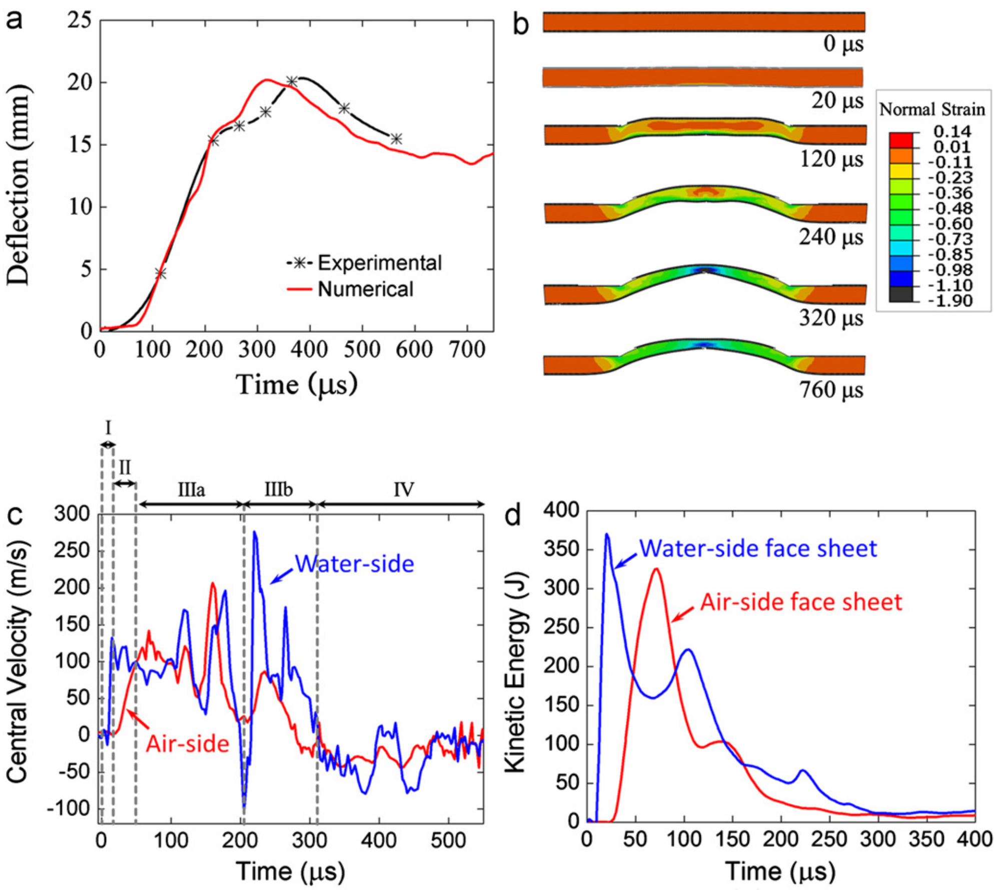

Fig. 6. (a) Comparison between the central deflection histories measured experimentally and predicted by numerical simulation for the sandwich composite panel at an impulse $I_0=5581$ Pa s. (b) Simulated deformation of the foam core represented as contour plots of Lagrangian normal strain in the panel thickness direction. (c) Plots of center-point velocity for the water-side and air-side face sheets vs. time. Stages I, II, IIIa, IIIb and IV are labeled to differentiate the dynamic responses of foam core, air-side and water-side face sheets. (d) Plots of kinetic energy of the water-side and air-side face sheets vs. time.

shear off at the clamped boundary. We start by comparing the numerically predicted central deflection history of the air-side face sheet with the experimentally measured result (see Fig. 6a). The ascending slope of central deflection predicted by the numerical model compares very well with the experiment. A maximum deflection of $\sim$20.2 mm and a final deflection of $\sim$14.0 mm are predicted, in good agreement with the experimental values of 20.1 mm and 15.5 mm. The spring-back rate after the panel deflection reached the maximum value predicted by the model correlates excellently with the test. Unlike the monolithic panel, which deforms elastically until a brittle failure, the plastic deformation of the foam core resulted in a slower spring-back rate and a larger residual deformation for the sandwich composite panel.

To better understand the extraordinary energy absorption capability of the sandwich composite panel, we investigated the role of each component during the deformation. The deformation history of the foam core is represented by plotting contours of the Lagrangian normal strain in the panel thickness direction in Fig. 6b. This demonstrates the unique energy dissipation mechanism of foam core crushing that is present in sandwich panels. Examining both the foam deformation history and the center point velocity histories of the air-side and water-side face sheets in Fig. 6c, we found slightly more complex deformation phases than those proposed in Fleck and Deshpande (2004) and Liang et al. (2007). Stage I (0–20 μs) is the initial fluid–structure interaction phase when the panel behaves similar to a free-standing plate. In this phase, the impulse impinges on the water-side face sheet and crushes a thin layer of the foam core behind it. Meanwhile, the air-side face sheet remains static. At the end of stage I, water cavitation begins. Stage II (20–40 μs) is the core compression phase in which the wave transmits through the whole panel and accelerates the air-side face sheet. Stage IIIa (40–220 μs) is the panel bending and stretching phase when the air-side face sheet moves at a velocity similar to that of the water-side face sheet with lateral waves traveling across the panel. Stage IIIb (220–310 μs) is the cavitation collapse and foam crushing phase in which the water bubble collapses and the foam core crushes. A large amount of energy is dissipated during this phase. Stage IV (after 310 μs) is the panel bending and stretching "recovery" phase when the foam and both the air-side and water-side face sheets behave similar to a solid plate. Spring-back of the panel is observed in this phase.

As expected, the numerical simulation helps to identify the sequence of various damage mechanisms in the sandwich panel. Fig. 7a shows the cross-sectional view of the sandwich panel from the simulation of the interface delamination and the contours of Lagrangian normal strain in the foam along the panel thickness direction. The panel deformation and foam compression contour correlate closely with the cross-sectional view of the specimen after the experiment. Furthermore, magnified views from

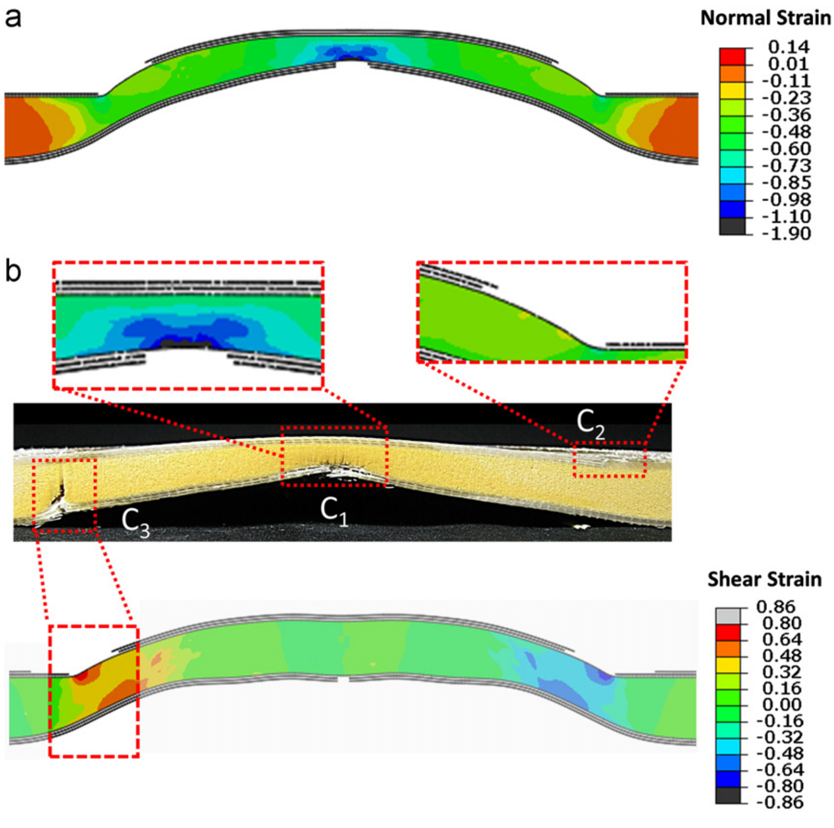

Fig. 7. (a) Cross-sectional view of the sandwich panel from the numerical simulation with contour plots of the Lagrangian normal strain in the foam in the panel thickness direction. (b) Cross-sectional view of the sandwich panel after a test showing three prominent damage regions, C_1, C_2 and C_3. Magnified views of the numerical simulation results for the corresponding regions are provided. For regions C_1 and C_2, contour plots of the Lagrangian normal strain for the foam in the panel thickness direction are given. For region C_3, the contour plot of the shear strain in the foam at 180 μs is given.

the numerical simulation of the three major damage regions (C_1, C_2 and C_3 in Fig. 7b) provide valuable insight into the damage processes. For instance, the compressive strain in the central region of the panel (C_1 in Fig. 7b) indicates a severe core crushing due to the cavitation collapse. A V-shaped compressive strain localization pattern in the foam matches two cracks observed experimentally that extend from the water-side face sheet surface at $\sim 45^{\circ}$. The water-side face sheet in region C_1 displays extensive delamination, matrix damage, and fiber rupture associated with the impulse induced by the water cavitation collapse. All these features are captured by the model. Moreover, by examining the air-side face sheet near the clamped boundaries (region C_2 in Fig. 7b), inter-lamina delamination is found in both experiment and simulation results. In addition, another important failure mechanism is identified: shear-off at the boundaries. As shown in Fig. 7d, one side of the sandwich panel at the clamped region exhibits failure in the foam beginning on the water-side face sheet (region C_3). The crack initiated from the bottom and propagated almost vertically up to the air-side face sheet. This is a typical shear-off failure feature, which is indicative of a failure mode in sandwich panels as suggested by Hutchinson and Xue (2005) where shear-off occurs very early in the history of the panel response prior to core crush and overall bending and stretching. This behavior is also observed in the present simulation, as is evident from the Lagrangian shear strain contour plot at 180 μs after impact, just before major foam core crushing in the boundary. Noteworthy is the fact that similar results were obtained in Wei et al. (in press) when Hashin's rate independent model was employed.

We next examine the model-predicted fiber and matrix damage patterns and compare them with the experimental measurements, Fig. 8, as well as those predicted in Wei et al. (in press). In Fig. 8b, an X-shaped fiber failure pattern is clearly present in the middle of the water-side face sheet. At the intersection of the "X", the fiber failed primarily as a result of rupture, whereas toward the end of the pattern, the fiber failed mainly by pull-out accompanied with matrix failure due to shear. In our previous study (Wei et al., in press), Hashin's failure criteria was applied for predicting the composite failure in the sandwich panel using the shear contribution factor $\alpha = 1$, see Eq. (7). An X-shaped fiber failure pattern was obtained, but the fiber damage level in the pattern was only 60%, far from full damage. Furthermore, fiber failure on circular sectors at the clamped edge was predicted. Such failure pattern is absent in the simulations with the new model in agreement with the experimental findings. In this case of the new model, fiber damage is predicted on the air-side face sheet along the boundary due to the constraint imposed by the steel ring. In the experiment, evidence of fiber damage in those regions was found; however, the damage level is slightly less than the model prediction. This discrepancy probably occurs because accurate damage modeling at the contact between the face sheet and the steel clamp ring would require a finer mesh to better describe the rounded edge of the steel ring.

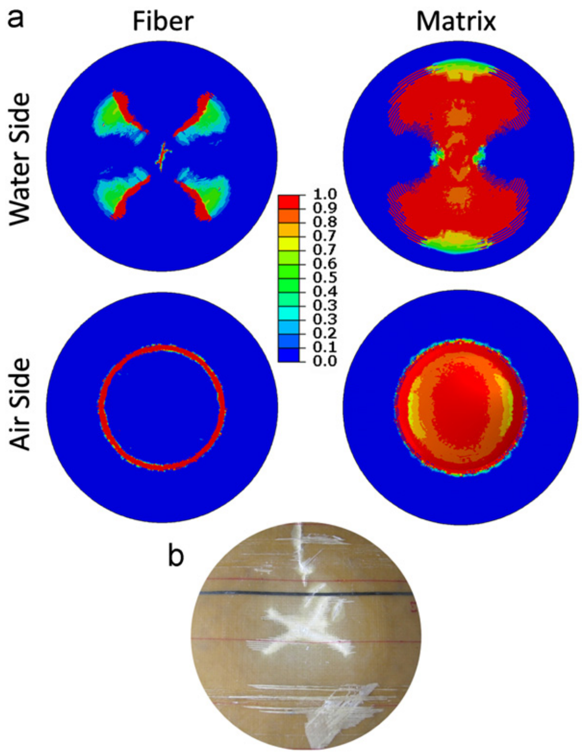

Fig. 8. (a) Model-predicted fiber and matrix damage patterns in the water-side and air-side face sheets (the damage variable from 0–1 represents the damage level from low to high); (b) photograph of the fiber failure pattern in the water-side face sheet of the sandwich composite panel (the black line denotes the fiber orientation in the first laminate on the water-side face sheet).

Another important feature revealed by the new numerical model is the matrix damage distribution in the air-side and water-side face sheets. As shown in Fig. 8a, a much more uniformly distributed matrix damage pattern is predicted for the air-side face sheet compared to the water-side face sheet because the foam core crushing dissipates a significant amount of energy and mitigates the impulse transmitted to the air-side face sheet. More importantly, in stages IIIa and IIIb, the foam core helps to homogenize the pressure on the air-side face sheet, which results in a uniform matrix damage pattern. When these patterns are compared to those reported in Wei et al. (in press), major differences are observed. Matrix damage is much more pronounced in the new model prediction on both water and air-side face sheets.

The predicted response of the sandwich composite panel, during the test, is shown in Video 1 (available online). The FSI model accurately captures water cavitation formation and its collapse. In addition, the formation of an X-shaped fiber failure pattern, which initiates by fiber pull-out, is clearly observed in the video. This shows that the new rate-dependent composite model has better predictive capabilities than previously formulated models.

Supplementary material related to this article can be found online at http://dx.doi.org/10.1016/j.jmps.2013.02.006.

4. Concluding remarks

Because of limitations exhibited by existing unidirectional composite models, we have developed a new rate-dependent unidirectional laminate model and applied it to simulate scaled fluid–structure interaction (FSI) lab experiments. The simulations used a coupled acoustic-solid technique capable of accurately describing the interaction between water and composite panels. The numerical model takes into account the strain-rate effect for the interlaminate interfaces, the foam core, and the fiber-reinforced composite laminates. The laminate model uses Hashin's fiber failure criterion and a modified Tsai–Wu matrix failure criterion. The composite moduli are degraded using five damage variables, which are updated in the post-failure regime by means of a linear softening law governed by an energy release criterion. A key feature in the formulation is the distinction between fiber rupture and pull-out by introducing a fracture toughness, which varies from a fiber tensile toughness to a matrix tensile toughness as a function of the ratio of longitudinal normal stress to effective shear stress. The experimentally validated failure criteria for unidirectional E-glass/vinylester composite plies were formulated and implemented into the FSI model. Rate-dependent damage initiation and evolution was accounted for in the model, providing a capability for differentiating between fibers rupture and pull-out failure mechanisms. The numerical model is able to depict the various material deformation and damage mechanisms observed in monolithic and sandwich composite panels, such as inter-lamina delamination, fiber and matrix damage, and foam crushing. All of the rate-dependent material properties discussed above have been shown to be important in damage initiation and evolution. The details given by the numerical simulations provide valuable insights into the material degradation process, as well as the key energy dissipation mechanisms present in composite panels. Validated by the underwater blast experiments, this numerical model can serve as a powerful tool to efficiently and accurately predict the performance of composite structures. Furthermore, by proper parameterization the rate-dependent unidirectional composite model can be applied to a variety of fiber/matrix combinations.

Acknowledgments

This research was carried out under the financial support of the Office of Naval Research (ONR) under grant number N00014-08-1-1055. We greatly appreciate the support and encouragement provided by Dr. Rajapakse throughout the study.

References

Abaqus 6.9-ef online documentation. 2009, Abaqus, Simulia.

Akil, Ö., Yıldırım, U., Güden, M., Hall, I., 2003. Effect of strain rate on the compression behaviour of a woven fabric s2-glass fiber reinforced vinyl ester composite. Polym.Test. 22 (8), 883–887.

Arora, H., Hooper, P., Dear, J., 2011. Dynamic response of full-scale sandwich composite structures subject to air-blast loading. Compos. A: Appl. Sci. Manuf. 42 (11), 1651–1662.

Arora, H., Hooper, P., Dear, J., 2012. The effects of air and underwater blast on composite sandwich panels and tubular laminate structures. Exp. Mech. 52 (1), 59–81.

Azzi, V., Tsai, S., 1965. Anisotropic strength of composites. Exp. Mech. 5 (9), 283–288.

Bakis, C.E., Bank, L.C., Brown, V.L., Cosenza, E., Davalos, J.F., Lesko, J.J., Machida, A., Rizkalla, S.H., Triantafillou, T.C., 2002. Fiber-reinforced polymer composites for construction-state-of-the-art review. J. Comp. Const. 6 (2), 73–87.

Benzeggagh, M., Kenane, M., 1996. Measurement of mixed-mode delamination fracture toughness of unidirectional glass/epoxy composites with mixed-mode bending apparatus. Compos. Sci. Technol. 56 (4), 439–449.

Camanho, P.P., Dávila, C.G., 2002. Mixed-mode decohesion finite elements for the simulation of delamination in composite materials. NASA-Tech. Pap., 211737.

Chaboche, J.L., 1981. Continuous damage mechanics–a tool to describe phenomena before crack initiation. Nucl. Eng. Des. 64 (2), 233–247.

Compston, P., Jar, P.Y.B., Davies, P., 1998. Matrix effect on the static and dynamic interlaminar fracture toughness of glass-fibre marine composites. Compos. B: Eng. 29 (4), 505–516.

Daniel, I., J. Cho, B. Werner, and J. Fenner, Mechanical behaviour and failure criteria of composite materials under static and dynamic loading. In: Proceeding of 17th International Conference on Composite Materials (ICCM17), 2009a.

Daniel, I.M., Luo, J.J., Schubel, P.M., Werner, B.T., 2009b. Interfiber/interlaminar failure of composites under multi-axial states of stress. Compos. Sci. Technol. 69 (6), 764–771.
Daniel, I.M., Ishai, O., Daniel, I., 1994. Engineering Mechanics of Composite Materials, vol. 22. Oxford University Press, New York.
Davila, C.G., Camanho, P.P., Rose, C.A., 2005. Failure criteria for frp laminates. J. Compos. Mater. 39 (4), 323–345.
Dear, J., Lee, H., Brown, S., 2005. Impact damage processes in composite sheet and sandwich honeycomb materials. Int. J. Impact. Eng. 32 (1), 130–154.
Dear, J.P., Brown, S.A., 2003. Impact damage processes in reinforced polymeric materials. Compos. A: Appl. Sci. Manuf. 34 (5), 411–420.
Donadon, M., Iannucci, L., Falzon, B., Hodgkinson, J., Almeida, S.De, 2008. A progressive failure model for composite laminates subjected to low velocity impact damage. Comput. Struct. 86 (11-12), 1232–1252.
Fleck, N.A., Deshpande, V.S., 2004. The resistance of clamped sandwich beams to shock loading. J. Appl. Mech. 71 (3), 386–401.
Hashin, Z., 1980. Failure criteria for unidirectional fiber composites. J. Appl. Mech., 32947, 329.
Hashin, Z., Rotem, A., 1973. A fatigue failure criterion for fiber reinforced materials. J. Compos. Mater. 7 (4), 448–464.
Hutchinson, J.W., Xue, Z.Y., 2005. Metal sandwich plates optimized for pressure impulses. Int. J. Mech. Sci. 47, 545–569.
Iannucci, L., Willows, M., 2006. An energy based damage mechanics approach to modelling impact onto woven composite materials—part i: Numerical models. Compos. A: Appl. Sci. Manuf. 37 (11), 2041–2056.
Kachanov, L.M., 1986. Introduction to Continuum Damage Mechanics, vol. 10. Springer.
Lapczyk, I., Hurtado, J.A., 2007. Progressive damage modeling in fiber-reinforced materials. Compos. A: Appl. Sci. Manuf. 38 (11), 2333–2341.
Latourte, F., Grégoire, D., Zenkert, D., Wei, X., Espinosa, H.D., 2011. Failure mechanisms in composite panels subjected to underwater impulsive loads. J. Mech. Phys. Solids 93 (11), 3072–3081.
LeBlanc, J., Shukla, A., 2011. Dynamic response of curved composite panels to underwater explosive loading: Experimental and computational comparisons. Compos. Struct.
Lee, D.G., Lim, T.S., Cheon, S.S., 2000. Impact energy absorption characteristics of composite structures. Compos. Struct. 50 (4), 381–390.
Liang, Y., Spuskanyuk, A.V., Flores, S.E., Hayhurst, D.R., Hutchinson, J.W., McMeeking, R.M., Evans, A.G., 2007. The response of metallic sandwich panels to water blast. J. Appl. Mech. 74 (1), 81–99.
Maimí, P., P.P. Camanho, J.A. Mayugo, and C.G. Davila, A thermodynamically consistent damage model for advanced composites. 2006.
Matzenmiller, A., Lubliner, J., Taylor, R., 1995. A constitutive model for anisotropic damage in fiber-composites. Mech. Mater. 20 (2), 125–152.
Naik, N., Yernamma, P., Thoram, N., Gadipatri, R., Kavala, V., 2010. High strain rate tensile behavior of woven fabric e-glass/epoxy composite. Polym. Test. 29 (1), 14–22.
Oguni, K., Ravichandran, G., 2001. Dynamic compressive behavior of unidirectional e-glass/vinylester composites. J. Mater. Sci. 36 (4), 831–838.
Porfiri, M. and N. Gupta, A review of research on impulsive loading of marine composites. Major accomplishments in composite materials and sandwich structures, 2010: 169–194.
Rowlands, R., 1985. Strength(failure) theories and their experimental correlation, 3. Elsevier Science Publishers B. V., Handbook of Composites pp. 71–125.
Roy, R., Sarkar, B., Bose, N., 2001. Impact fatigue of glass fibre-vinylester resin composites. Compos. A: Appl. Sci. Manuf. 32 (6), 871–876.
Shokrieh, M.M., Omidi, M.J., 2009a. Compressive response of glass-fiber reinforced polymeric composites to increasing compressive strain rates. Compos. Struct. Res 89 (4), 517–523.
Shokrieh, M.M., Omidi, M.J., 2009b. Investigation of strain rate effects on in-plane shear properties of glass/epoxy composites. Compos. Struct. 91 (1), 95–102.
Shokrieh, M.M., Omidi, M.J., 2009c. Tension behavior of unidirectional glass/epoxy composites under different strain rates. Compos. Struct. 88 (4), 595–601.
Sun, C., 2000. Strength analysis of unidirectional composites and laminates. Compr. Compos. Mater. 1, 641–666.
Tijssens, M.G.A., Sluys, B.L.J., van der Giessen, E., 2000. Numerical simulation of quasi-brittle fracture using damaging cohesive surfaces. Eur. J. Mech. Ser. A Solids 19 (5), 761–780.
Tsai, S.W., Wu, E.M., 1971. A general theory of strength for anisotropic materials. J. Compos. Mater. 5 (1), 58–80.
Wei, X., Tran, P., Vaucorbeil, A.d., Ramaswamy, R.B., Latourte, F., Espinosa, H.D. Three-dimensional numerical modeling of composite panels subjected to underwater blast. J. Mech. Phys. Solids. http://dx.doi.org/10.1016/j.jmps.2013.02.007, in press.